Baryon stopping and charge deposition in heavy-ion collisions due to gluon saturation

Oscar Garcia-Montero^{1,*} and Sören Schlichting¹

¹Fakultät für Physik, Universität Bielefeld, D-33615 Bielefeld, Germany

(Dated: September 17, 2024)

We compute baryon and electric charge deposition in high-energy heavy-ion collisions using the Color Glass Condensate (CGC) Effective Field Theory, where at leading order charge is deposited through multiple scatterings of valence quarks with a saturated gluon target. A simplified phenomenological formula is derived to describe charge deposition, from which the parametrical dependence with collisional energy and geometry can be extracted. We present an approximate analytical prediction of the so-called baryon stopping parameter α_B , which shows excellent agreement with the state-of-the art extractions of α_B from experimental data. These results are further validated using the McDipper framework, by computing charge deposition at midrapidity across a range of collision energies ($\sqrt{s_{\rm NN}}$ = 62.4 – 5020 GeV).

I. INTRODUCTION

In heavy-ion collisions a large number of protons and neutrons collide into each other, forming a deconfined state of quarks and gluons, the so-called Quark Gluon Plasma (QGP). Net baryon number, B, as well as net electric charge, Q, are conserved quantities in nature which means that the total integrated charges are also conserved during heavy-ion collisions (HIC). During the very first instants of the collision, these conserved quantities are distributed throughout the newly formed QGP, leaving imprints across the transverse plane, with nontrivial longitudinal structures [1–5]. Even though the densities of all conserved quantities evolve via advection and diffusion throughout the lifetime of QGP; the longitudinal structures observed in the final state are believed to be intimately conected to the initial conditions [6, 7]. Hence, to understand the production of particles with these two quantum numbers, it is essential to understand the mechanism for charge deposition in the initial stage of the collision.

Developing a first principles understanding of the initial net charge deposition is particularly relevant to the Beam Energy Scan (BES) program at RHIC [8], which focuses on the creation of hot nuclear matter at nonvanishing baryon charge, which is achieved by colliding heavy ions at low and intermediate energies. These collisions explore different trajectories in the QCD phase diagram, effectively sweeping over it to find signatures of the QCD critical point and/or a first order QCD phase boundary. While these searches are performed at centerof-mass erngies $\sqrt{s}_{NN} \leq 200 \text{GeV}$, they can be complemented through searches at higher energies but quite forward/backwards rapidities, where baryon densities are also expected to be high [9-12]. One advantage of such high-energy forward searches is that models describing the QCD matter deposition into the fireball are in general better constrained theoretically. The advent of next

generation LHC detectors such as the Forward Calorimeter in ALICE (FoCal), the major upgrade ALICE 3 and the upgrades in settings of ATLAS, CMS and LHCb will allow the community to explore the physics of the large rapidity regions further, [13–15]. Therefore, understanding baryon stopping at intermediate and high collisional energies becomes a necessity.

Net baryon or – as a proxy – net proton rapidity distributions reveal information about the baryon stopping mechanism, i.e. how nucleons - and the associated baryon number- is decelerated from the initial beam rapidity towards the mid-rapidity region. By looking at these distributions along different energies [16, 17], one observes the appearance of a double-peaked structure with long tails towards the midrapidity region, with the maxima of baryon number deposition shifting to higher rapidities with increasing energy (c.f. Fig. 1). It is precisely this shift of the distributions, and therefore of the midrapidity tails which effectively causes the decrease in deposition power at midrapidity with increasing center of mass energy $s_{\rm NN}$. In the literature, a diverse array of mechanisms of baryon stopping have been discussed, including hadronic transport [18–20], Markovian processes in QCD [21] as well as mechanical deceleration mechanisms of string dynamics [22]. In recently years, the so called baryon junction, a topological configuration of gluons inside baryons [23] has received increasing attention, due to its potential in accounting for certain features of baryon charge deposition in high-energy collisions [24, 25]. Also in recent literature, this mechanism has been contrasted exclusively to the deposition of charge through perturbative scattering of valence quark from the projectile with the target. It is important to note that this a limit used traditionally by event generators such as Pythia [26, 27], POWHEG [28] and HERWIG[29], which fails to account for the observed baryon charge deposition, as brought to attention in a recent paper by Lewis et al. (see Ref. [30]).

In this paper, we present an alternative picture of netcharge deposition in heavy-ion collision, by re-imagining the perturbative quark scattering in the context of a saturated target. For this, we computed charge deposition using the Color Glass Condensate Effective Field Theory

^{*} garcia@physik.uni-bielefeld.de

(CGC EFT) at leading order (LO), where B and Q are deposited via multiple scatterings of single valence quark with a densely populated gluon target [31]. We present a simplified formula, derived from the single quark production which can easily be adapted to other phenomenological approaches, such as e.g. the TrENto initial state model [32], or MC-Glauber 3D [33] and thus be used for phenomenological purposes. Based on a reasonable set of assumptions, the net quark density can be computed as the sum of two contributions,

$$(n_{q_f}\tau)_0 = (n_{q_f}\tau)_{0,A\to B} + (n_{q_f}\tau)_{0,B\to A}$$
 (1)

corresponding to the -forward- charge deposited from the quarks q_f of nucleus A/B scattering off the saturated target B/A. Each individual contribution is given by

$$(n_{q_f}\tau)_{0,A\to B} = \sum_{h=p,n} x_1 q_{v_f/h} (x_1, Q_{s,B}^2(x_2, T_B(x))) T_{h/A}(\mathbf{x})$$
(2)

where $x_1q_{v_f/h}$ is the collinear parton distribution of the valence quarks of flavor f in hadron h, and $T_{h/A}$ denotes the thickness function of the hadron h in nucleus A. Due to kinematics the longitudinal momentum fractions $x_{1/2}$ are approximately given by

$$x_{1/2} \simeq Q_s^B / \sqrt{s_{NN}} e^{\pm \eta} \tag{3}$$

with the saturation scale $Q_{s,B}$ of nucleus B selfconsistently determined from a phenomenological parametrization $Q_{s,B}^2(x_2,T_B(x))$. The beauty of this formula is that the kinematic variables and the scale at which we are probing the quarks are fully determined by the characteristic scale of the gluon distribution of nucleus B, namely the saturation scale Q_B^2 . Based on this formula we obtain an analytic expression for the behavior of charge deposition at midrapidity, which is consistent with the trends in experimental data [30], We further investigate the behavior of baryon deposition using numerical event-by-event studies of the McDipper [34, 35] intitial state, which is based on the k_T -factorized limit of the CGC. We explore the systems size and collisional energy dependence, finding promising results for the latter.

This paper is organized as follows: in Section II we introduce the 3D quark charge stopping mechanism as given in the McDipper model. Additionally, we derive, based on kinematic arguments a simplified formula which can be used parametrically for initial charge deposition in phenomenological studies. In Section III we present results for initial baryon and electric deposition using the McDipper code. More specifically, we discuss baryon stopping as an energy of collisional energy in Section III A, while exploring its dependence on system size in Section III B. We finalize with our summary and conclusions.

II. 3D BARYON AND ELECTRIC CHARGE DEPOSITION IN THE MCDIPPER

Below we discuss the charge deposition in the so-called hydrid formalism of the CGC EFT [36–38] as implemented for valence quarks in the McDipper initial state model [34]. Within this framework net charge density is deposited via multiple scatterings of valence quarks in a dense gluon field. The average net quark charge density n_{q_f} can be extracted from the single (anti-)quark distributions,

$$(n_{q_f}\tau)_0 = \int d^2\mathbf{p} \left[\frac{dN_{q_f}}{d^2\mathbf{x}d^2\mathbf{p}dy} - \frac{dN_{\bar{q}_f}}{d^2\mathbf{x}d^2\mathbf{p}dy} \right]_{y=\eta_s}$$

$$= \int d^2\mathbf{p} \left[\frac{dN_{q_{f,V}}}{d^2\mathbf{x}d^2\mathbf{p}dy} \right]_{y=\eta_s} .$$

$$(4)$$

where at LO in the CGC power counting, the valence quark yield is given by [31, 39]

$$\frac{dN_{q_{f,V}}}{d^{2}\mathbf{x}d^{2}\mathbf{p}dy} = \frac{x_{1}q_{v_{f}/A}(x_{1}, \mathbf{p}^{2}, \mathbf{x}) \ D_{\text{fun}}^{(B)}(x_{2}, \mathbf{x}, \mathbf{p})}{(2\pi)^{2}} + \frac{x_{2}q_{v_{f}/B}(x_{2}, \mathbf{p}^{2}, \mathbf{x}) \ D_{\text{fun}}^{(A)}(x_{1}, \mathbf{x}, \mathbf{p})}{(2\pi)^{2}}.$$
(5)

with the kinematic variables $\{x_i\}$ are given by

$$x_{1/2} = \frac{\mathbf{p}}{\sqrt{s_{NN}}} e^{\pm y} \tag{6}$$

The result in Eqs. (4) and (5) is a result of the linear dependence of the charge deposition on the nuclear (anti-)quark parton distribution in the single quark production formulas at LO, as expressed in as [31, 39]¹

Intuitively, Eq. (5) states that valence charge is deposited into the interacting medium via the deflection of a collinear quark through multiple scatterings [40, 41] as illustrated schematically in Fig. 1. Different terms in Eq. (5) correspond to the stopping of valence charge contained in nucleus A or B; the first one refers to the valence quarks from the right moving nucleus (A) being deflected towards the forward cone, while the second term refers to left moving collinear quarks from nucleus B, being deflected to the backwards cone. While this may look symmetric (in the case of same-species collisions), as soon as there are fluctuations, charge deposition will fluctuate on an event-by-event basis depending on the positions of the nucleons.

In this work, the collinear quark nuclear PDFs, $q_{v_f/A}(x_{1/2}, Q^2, \mathbf{x})$, are given by scaling the independent

Note that this is true for the average charge deposition, i.e. as long as event-by-event fluctuations of the quark content of colliding hadrons are not taken on account.

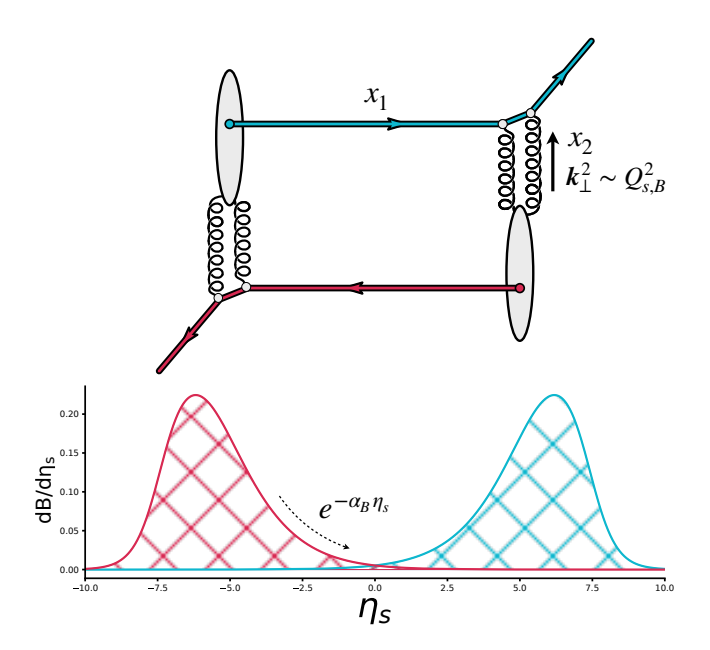


Figure 1: Charge deposition mechanism through baryon stopping in the saturation regime.

nucleonic PDFs, with the nuclear thickness functions $T_{p/n}(\mathbf{x})$ of protons/neutrons, i.e.

$$u_{A}(x, Q^{2}, \mathbf{x}) = u_{p}(x, Q^{2}) T_{p}(\mathbf{x}) + u_{n}(x, Q^{2}) T_{n}(\mathbf{x}),$$

$$d_{A}(x, Q^{2}, \mathbf{x}) = d_{p}(x, Q^{2}) T_{p}(\mathbf{x}) + d_{n}(x, Q^{2}) T_{n}(\mathbf{x}), \quad (7)$$

$$s_{A}(x, Q^{2}, \mathbf{x}) = T_{p}(\mathbf{x}) s_{p}(x, Q^{2}) + T_{n}(\mathbf{x}) s_{n}(x, Q^{2}).$$

As in Ref. [34], we will assume isospin symmetry, as the parton distributions of the neutron are not well constrained. This in turn means that the neutron PDFs are set to the proton PDFs after the transformation $u \leftrightarrow d$, i.e. $u_{p/n} = d_{n/p}$, such that Eq. (7) simplifies to

$$u_A(x, Q^2, \mathbf{x}) = u(x, Q^2) T_p(\mathbf{x}) + d(x, Q^2) T_n(\mathbf{x}),$$

$$d_A(x, Q^2, \mathbf{x}) = d(x, Q^2) T_p(\mathbf{x}) + u(x, Q^2) T_n(\mathbf{x}), \quad (8)$$

$$s_A(x, Q^2, \mathbf{x}) = (T_p(\mathbf{x}) + T_n(\mathbf{x})) s(x, Q^2).$$

Finally, the last ingredient of the charge deposition is the fundamental dipole gluon distribution, $D_{\text{fun}}^{(A/B)}$ of nucleus A/B,

$$D_{\text{fun}}(x, \mathbf{x}, \mathbf{q}) = \frac{1}{N_c} \int_{\mathbf{s}} \text{tr}_{\text{fun}} [U_{\mathbf{x} + \mathbf{s}/2} U_{\mathbf{x} - \mathbf{s}/2}^{\dagger}] e^{i\mathbf{q} \cdot \mathbf{s}}$$
(9)

which corresponds to scattering cross section of a quark in the Color Glass Condensate formalism of high-energy scattering.

A. Parametrical formula

Now that we have established the theoretical basis, the main objective of this subsection is to develop a simple and intuitive formula that can be used for phenomenological purposes. For this, we will use the simplest model available, the Golec-Biernat Wusthoff (GBW) model [42–44], where the fundamental dipole gluon distribution is given by a Gaussian distribution around the saturation scale,

$$D_{\text{fun}}(\mathbf{x}, \mathbf{q}) = \frac{4\pi}{Q_F^2(x, \mathbf{x})} \exp \left[-\frac{\mathbf{k}^2}{Q_F^2(x, \mathbf{x})} \right]. \tag{10}$$

where Q_F is the saturation scale in the fundamental representation. The kinematic dependence of Q_F is given phenomenologically by the relation [42]

$$Q_F^2(x, \mathbf{x}) = Q_{p,0}^2 x^{-\lambda} (1 - x)^{\delta} (T_p(\mathbf{x}) + T_n(\mathbf{x})) \sigma_0,$$
 (11)

where $Q_{p,0}^2 = 0.152\,\mathrm{GeV}^2$, $\lambda = 0.215$, $\sigma_0 \equiv 2\pi B_G$ denotes the effective transverse area of the nucleon. This means that $(T_p(\mathbf{x}) + T_n(\mathbf{x}))\sigma_0$ counts the density of nucleons per unit transverse area. In this work, $\delta = 1$ is introduced to regulate the large x behavior. In what follows, we will drop the fundamental representation index in favor of labeling the nucleus it refers to, e.g. $Q_{A/B}^2$ for nucleus A/B.

In the interest of keeping this derivation simple, we will focus only on the charge being deposited into the forward region (from projectile A to target B), corresponding to the first term of Eq. (5). The case for the backward deposited charge is, naturally, analogous to these computations and can be obtained by switching nucleus A for nucleus B and inverting rapidity. For the case of forward charge, the quark number density, deposited via multiple scatterings of the collinear quarks of nucleus A with the gluon distributions of nucleus B, is then simply described by

$$(n_{q_f}\tau)_{0,A\to B} = \int \frac{\mathrm{d}^2\mathbf{p}}{(2\pi)^2} x_1 q_{v_f/A}(x_1, \mathbf{p}^2, \mathbf{x}) D_{\text{fun}}(x_2, \mathbf{x}, \mathbf{p})$$
(12)

By using the assumption of isospin symmetry for the proton and neutron PDFs, the $A \rightarrow B$ charge is given by

$$(n_u \tau)_{0,A \to B} = \nu_{u,A \to B} T_{p,A}(\mathbf{x}) + \nu_{d,A \to B} T_{n,A}(\mathbf{x})$$

$$(n_d \tau)_{0,A \to B} = \nu_{d,A \to B} T_{p,A}(\mathbf{x}) + \nu_{u,A \to B} T_{n,A}(\mathbf{x}),$$
(13)

where we have used Eq. (7) to decompose the relation into the individual collinear quark distributions for each quark flavor. We have expressed the resulting integrals as

$$\nu_{f,A\to B} = \int_0^\infty \frac{\mathrm{d}^2 \mathbf{p}}{(2\pi)^2} \, x_1 q_{v_f/p}(x_1, \mathbf{p}^2) \, D_{\text{fun}}(x_2, \mathbf{x}, \mathbf{p}) \,. \tag{14}$$

Now since at any given value of x, the dipole distribution is dominated by momenta $\mathbf{p}^2 \sim Q_B^2$, whereas the \mathbf{p}^2 dependence of the collinear quark distribution is only logarithmic due to DGLAP evolution, we can approximate

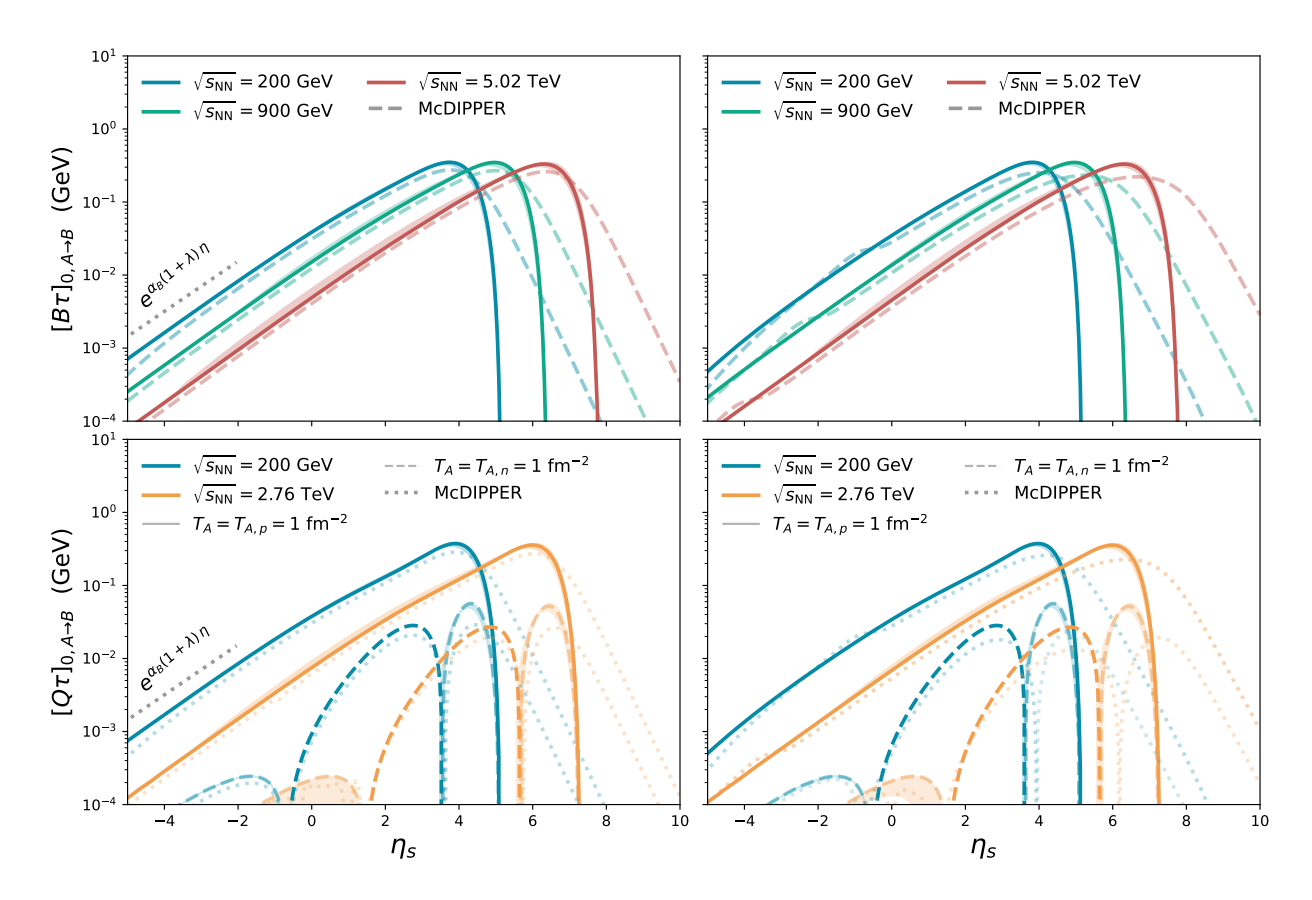


Figure 2: Comparison of baryon (upper panels) and electric charge deposition (lower panels) for two different energies, 200 GeV and 2.76 TeV. The (left) panels correspond to the gaussian GBW model, while the (right) panels correspond to the IP-Sat model, where the effective Q_s^2 is extracted from the dipole function as explained in the main text.

the integral in Eq. (14), by setting $\mathbf{p}^2 = Q_B^2(x_2)$ in the PDF, and approximating the kinematics by

$$x_{1/2} \simeq \frac{Q_B(x_2, \mathbf{x})}{\sqrt{s_{NN}}} e^{\pm y} \tag{15}$$

as long as the $x_{1/2}$ dependence is sufficiently mild. By virtue of this approximation, the PDF factorizes and the **p** integration of the dipole gluon distribution yields unity, as the reader can deduce from the definition in Eq. (9). We then obtain

$$\nu_{f,A\to B} \approx x_1 q_{v_f/p}(x_1, Q_B^2),$$
 (16)

where in the GBW Model, the self-consistent solution to x_1 and x_2 are given by

$$x_1 = \left[\frac{Q_{p,0}^2}{s_{\text{NN}}} T_B(\mathbf{x}) \, \sigma_0 e^{2y(1+\lambda)} \right]^{1/(2+\lambda)} . \tag{17}$$

$$x_2 = \left[\frac{Q_{p,0}^2}{s_{\text{NN}}} T_B(\mathbf{x}) \, \sigma_0 e^{-2y} \right]^{1/(2+\lambda)} \,. \tag{18}$$

Next, in order to develop a more analytical feeling to this formulas, we will assume a functional form for the PDFs, following Ref. [45]. Since more complex parametrizations primarily affect the large-x regions, we use the simple parametrization

$$xq_{v_f/p}(x,Q^2) = a_0(Q^2)x^{a_{1,f}(Q^2)}(1-x)^{a_{2,f}(Q^2)}$$
 (19)

where the exponents $a_{1,f}, a_{2,f}$ and the normalization $a_{0,f}$ typically exhibit a very mild dependence on Q^2 (slower than logarithmic) and the exponents $a_{1,f}$ and $a_{2,f}$ are not equal for u and d, albeit being close in value. By plugging this functional form into Eq. (16), we get

$$\nu_{f,A \to B} \approx a_0 x_1^{a_{1,f}} \tag{20}$$

which naturally give a parametrical dependence on energy and thickness due to Eq. (17). These dependencies can be explicitly given by

$$\nu_{f,A\to B} \sim T_B^{\frac{a_{1,f}}{2+\lambda}} s_{\text{NN}}^{-\frac{a_{1,f}}{(2+\lambda)}} \exp\left[2ya_{1,f} \frac{1+\lambda}{2+\lambda}\right]$$
(21)

In high-energy kinematics $\sqrt{s_{\rm NN}} \gg m_N$ the beam rapidity is approximately given by $y_{\rm beam} \approx \log(s_{\rm NN}/m_N^2)/2$,

such that upon inverting this relationship and plugging it into Eq. (21) we obtain

$$\nu_{f,A\to B} \sim T_B^{\frac{a_{1,f}}{2+\lambda}} \exp\left[-\alpha_B(y_{\text{beam}} - y(1+\lambda))\right]$$
 (22)

where we define the prefactor inside the exponential as our parametrical baryon stopping parameter,

$$\alpha_B \approx \frac{2a_{1,f}}{2+\lambda} \,.$$
 (23)

By inserting the parameters for the GBW model, and the fits to the x^{a_1} tails in the CT18NNLO PDF sets, ² we find that $\alpha_B \approx 0.5 - 0.7$, which is remarkably different from the value of $\alpha_{B/Q} \approx 2$ that one obtains in collinearly factorized pQCD calculations (c.f. Appendix A).

We will now validate this approximate expression, by comparing it to a numerical evaluation of the charge deposition in the McDipper framework. In Fig. 2, we present a direct comparison, which has been performed for two different dipole models: on the left we present results for the GBW model, for which the formula is explicitly derived above, while on the right the comparison is presented for the well known IP-Sat model. Indeed, we find that the common features of charge deposition as presented in Ref. [34] are well reproduced by the analytical formula. The tail towards midrapidity and the rapidity shift due to the increasing collisional energies are well described. Nevertheless, for very forward rapidities there is a bigger discrepancy between the phenomenological formula, Eq. (16), and the full result. The lack of an exponential tail at high rapidities in the parametrical approximation can be traced back to the saddle point approximation leading to Eq. (16). At such high rapidities, transverse momenta at the saturation scale become kinematically prohibited, whereas contributions from modes with $\mathbf{p} \lesssim Q_B^2$ are still allowed by the integration in the full formula. The rapid decay of the charge deposition in the approximated case is due to the lack of the contribution from these low momentum modes.

By looking at Eq. (22), it is easy to see that the overall trend is that denser matter has an antagonistic -and lesser- effect on the charge deposition. This not only means that denser regions of the collision deposit more charges, as expected, but also that denser hotspots move the peak of production closer to midrapidity than more dilute cases. This coincides with the intuitive picture of the quarks being stopped more effectively by a denser wave-packet of glue.

Different solid/dashed lines in Fig. 2 correspond to two different isospin configurations for the deposition for the forward charge deposition. Solid lines show the baryon and charge densities for $T_A = T_{p,A} = 1 \text{fm}^{-2}$ (and thus

 $T_{n,A} = 0$), while the second configuration of the incoming projectile, shown in dashes, is taken to have only neutron density. These configurations are supposed to roughly mimic the valence quarks of a proton or a neutron scattering through a general target, for which we have chosen $T_B = 1 \text{fm}^{-2}$, as in Eq. (10) and Eq. (11) the isospin composition of the target is irrelevant. We observe that, as expected, the deposition of baryon charge is completely unaffected by the isospin flip of the configuration. On the other had, the electric charge deposited by the quasi $n \to p$ configuration presents a completely different rapidity profile as the $p \to p$ configuration due to the different quark content. The picture that emerges is then that in the saturation picture, charges are contained by the valence quarks, and the baryon stopping is performed by the coherent wavepacket in the target. Intuitively, quarks are just being stopped by scattering through a wall of gluons. This is supported by the fact that diluting of the target $Q_{p,0}^2 \to 0$ shifts the peak to larger rapidities, and reduces the charge deposited at midrapidity. This can be easily seen from Eq. (17), where decreasing $Q_{n,0}^2$ is effectively the same as increasing s_{NN} .

The right panels of Fig. 2 explore a comparison of the approximated formula to the IP-Sat model [43]. In the IP-Sat model, however, the dipole function is Gaussian only at small transverse momentum, and in general, nongaussianities affect the deposition of charge and energy. However, while the saturation scale is not explicitly defined in the IP-Sat model as in the GBW model, the gluon distribution is indeed highly peaked at a value p_{\perp}^* , which is the requirement for the computation of the approximated formula. By following standard procedure [46], an effective saturation scale can then be extracted by defining the saturation scale in analogy to the GBW, such that Q_S is given implicitly by

$$D_{\text{fun}}(x, \mathbf{x}, Q_S^{-1}(x, \mathbf{x})) \equiv e^{-1/4}$$
. (24)

Even with the non-gaussianities present in the IP-Sat model, the qualitative agreement in Fig. 2, is still remarkable; in particular the description of the small η_s tail is still completely captured by the approximate formula. Because this approximation only depends on the dipole being a highly peaked distribution, we propose that the general parametrization in Eqs. (1) and (2) can be used for baryon and electric charge depositions in heavy ion collisions, and only needs to be supplemented with a suitable scheme to provide the effective satuation scale $Q_s(x, T(\mathbf{x}))$ as a function of momentum fraction x and nuclear thickness $T(\mathbf{x})$.

III. PHENOMENOLOGICAL IMPLICATIONS OF THE CHARGE DEPOSITION

Now that we have described the underlying physical picture and obtained a simple analytic description, we continue to perform a more comprehensive analysis of electric and baryon charge deposition at midrapidity in

² Since the valence quark distribution is very well constrained, other PDF sets leave the baryon(electric) charge almost unaffected, as it was shown in Ref. [34].

the context of the McDipper model. The analysis here presented will focus on two aspects: collisional energy (beam rapidity) and system size dependence at midrapidity, which is meant to directly address the recent measurements by STAR and ALICE [47–50].

A. Baryon stopping as a function of center-of-mass energy

In Fig. 3 we present the excitation of function for baryon (left) and electric (right) charge deposition in Au-Au collisions at midrapidity ($|\eta_s| < 0.5$) for a wide energy range, $62.4\,\mathrm{GeV} \leq \sqrt{s_\mathrm{NN}} \leq 5020\,\mathrm{GeV}^3$. It is important to note that we have fixed the species to $^{197}\mathrm{Au}$ to avoid including system size effects in baryon deposition which may muddle the extraction of the behavior. Additionally, it is worth noting that we have restricted ourselves to energies above $\sqrt{s_\mathrm{NN}} > 62.4\,\mathrm{GeV}$ to keep the kinematic variables (e.g. x_2) for forward deposition inside the range of validity of the CGC EFT. Nevertheless, we note in passing that previous work using the hybrid formalism explores quark deposition at low and intermediate energies (6-60 GeV) [51], and found a good agreement for the position of the peaks of the baryon rapidity density.

We follow previous works [13, 30, 52] and present these results as a function of the rapidity shift, $\delta y = y - y_{\text{beam}}$, where we report an exponential decrease of charge deposition with respect to δy , both for the electric and baryon charge deposition. As it is expected parametrically for midrapidity,

$$\frac{\mathrm{d}Q_i}{\mathrm{d}\eta_s}\bigg|_{|\eta_s|<0.5} \propto e^{\alpha_B (\eta_s - y_{\mathrm{beam}})} \tag{25}$$

with $Q_i = [B, Q]$. We fit the slope of the computed charges using Eq. (25). The function with the fitted data is given by the gray dotted lines in Fig. 3. In Fig. 4 the reader can find the baryon and electric charge stopping parameters, α_B and α_Q respectively, as a function of the centrality class up to the 70–80%. When averaged across all centralities, they yield

$$\alpha_B = 0.69 \pm 0.01$$
 and $\alpha_Q = 0.70 \pm 0.01$, (26)

which is fully consistent with the semi-analytical result. While the numbers presented here are for the initial baryon charge, and not for the final net-proton, as it was presented in Ref. [30], the baryon stopping parameters computed with the McDipper are quite close to the measured exponents. Because this is such a coarse-grained observable, we also do not expect that the hydrodynamical evolution will exert an important change in the overall trend, albeit this remains to be checked by

performing full event-by-event initial state + hydrodynamic +afterburner simulations, as we intend to do in the future.

We finally note that the inclusion of saturation effects in the form of transverse momentum transfer from the target gives rise to an exponent α_B , that is quite different from results the values expected for collinear factorisation where $\alpha_B \approx 2$ is much larger (c.f. Appendix A). Indeed, it has been reported that previous implementations of collinear factorization and string dynamics without extra assumptions fails to reproduce the $s_{\rm NN}$ of the data [24]

B. System size and charge deposition

Next, we explore the effect of system size on the deposition of conserved charges. For this, we ran a collection of species, where in order to avoid including spurious geometrical effects such as fluctuations due to deformations, we have chosen only species in which a spherical Woods-Saxons profile parametrization is known. The species ran were ${}^{16}_{8}$ O, ${}^{40}_{18}$ Ar, ${}^{63}_{29}$ Cu, ${}^{96}_{40}$ Zr, ${}^{129}_{54}$ Xe, ${}^{197}_{79}$ Au and ${}^{200}_{82}$ Pb, while varying the collisional energy for $\sqrt{s_{\mathrm{NN}}}$ = [200, 900, 5020] GeV. For simplicity of presentation, we only show the baryon deposition for collisions at 5.02 TeV in Fig. 5, but a very similar trend can be found for the other energies. We note that while the baryon charge may be compared across different A's, the electric charge needs to be compared instead to the number of initial protons, Z, since the ratio A/Z changes with species. In Fig. 5 (top) we can observe that the deposited baryon charge follow an increase with increasing system size A, which can be represented as

$$\frac{\mathrm{d}B}{\mathrm{d}\eta_s}\Big|_{|\eta_s|<0.5} \approx A^{\gamma_B} \quad \text{and} \quad \frac{\mathrm{d}Q}{\mathrm{d}\eta_s}\Big|_{|\eta_s|<0.5} \approx Z^{\gamma_Q} . \quad (27)$$

We have fitted the data to Eq. (27). The exponents γ_{Q_i} can be found in Fig. 5 (below) for different centralities and collisional energies. The exponents are consistent with each other across collisional energies. This is a consequence of the isospin symmetry which we have introduced in Eq. (8).

IV. CONCLUSIONS

We have presented a simplified formula for quark density deposition based on the hybrid formalism of the CFC EFT. The formula samples quarks from collinear PDFs while the scales at which they are sampled are set by the properties of the unintegrated gluon distributions of the nucleus being probed by the traversing valence quark. We found that the formula gives remarkably good results for small and intermediate rapidities, and only deviates from the full result in the fragmentation region very close to the beam rapidity.

³ For a discussion on the total charge deposited, the reader can refer to Ref. [35]

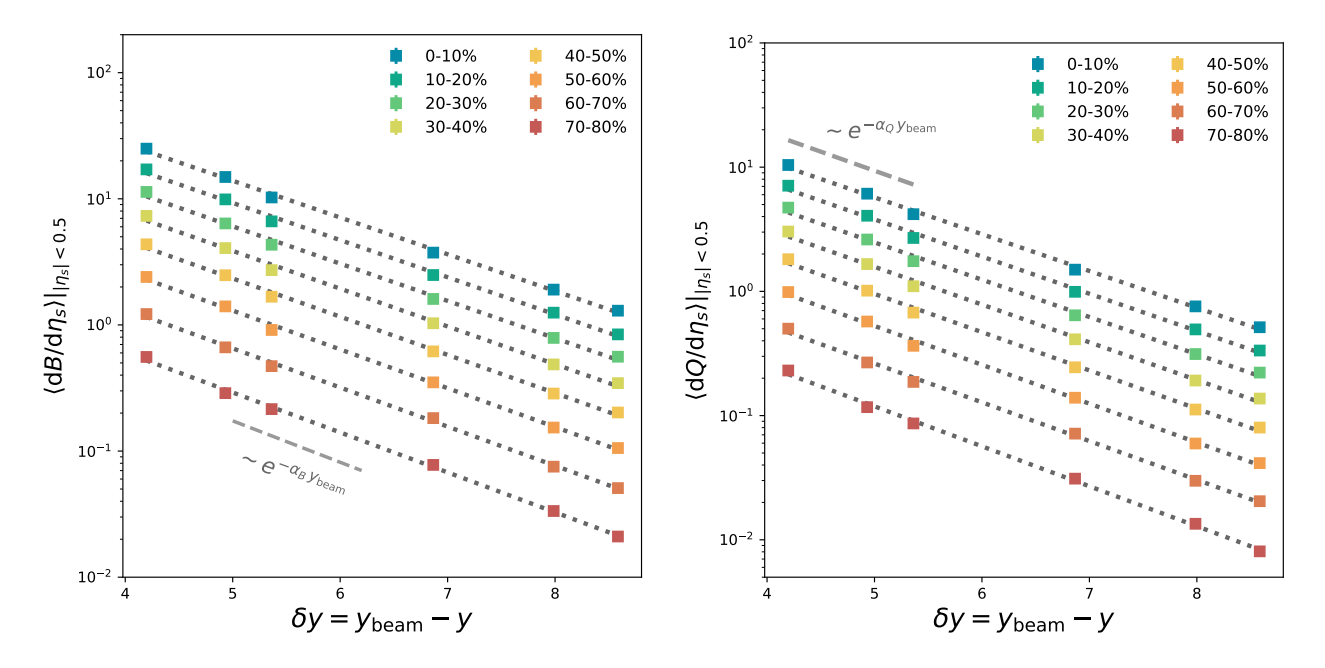


Figure 3: Midrapidity baryon charge (*left*) and electic charge (*right*) deposition as a function of collisional energy, $\sqrt{s_{\mathrm{NN}}}$. The deposited charge follows a power law $s_{\mathrm{NN}}^{\alpha_i/2}$ with i = [B, Q], or equivalent, an exponential with the rapidity shift, y_{beam} .

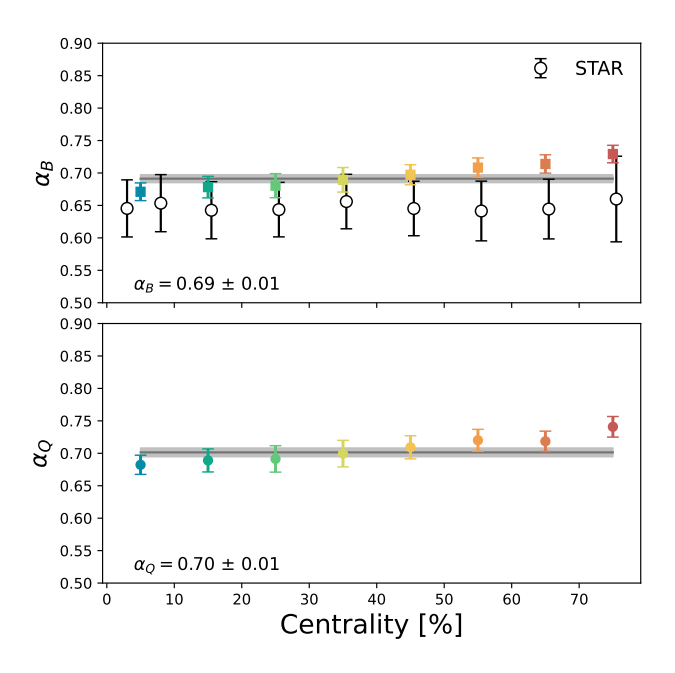


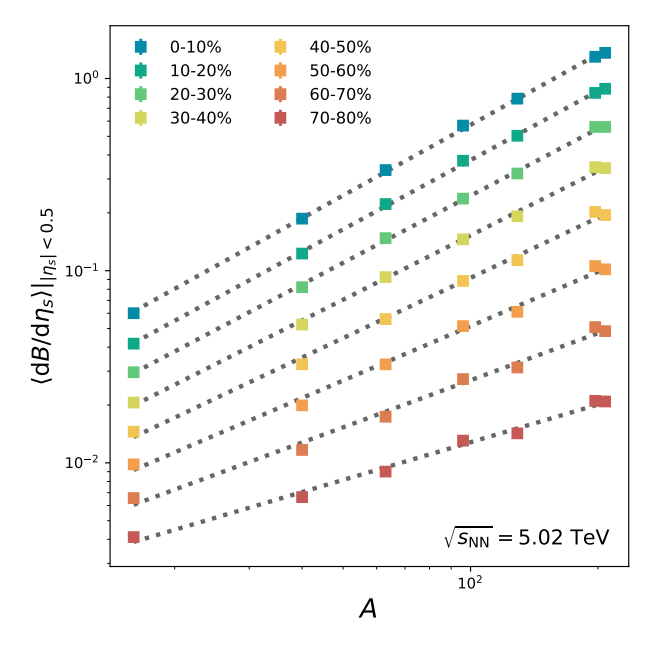
Figure 4: Baryon stopping parameters as extracted from data from the McDipper initial state model as compared to the extracted experimental values from STAR [52]. The gray line corresponds to our theoretical centrality-averaged value.

We also presented a phenomenological study on the initial baryon and electric deposition of the McDipper, where we have studied the collisional energy and system

size dependence of the deposited charge, for a variety of centralities. We show that the $\sqrt{s_{\rm NN}}$ dependence is consistent with the dependence extracted from experiment [30] at intermediate energies. On the other hand, the study of charge deposition with respect to system size shows that baryon and electric charge deposited in the midrapidity increase as a power law with the total nucleon number $(A^{\gamma_{B/Q}})$. Nevertheless, the specific power $\gamma_{B/Q}$ presents an extra centrality dependence.

Since the McDipper provides a rather successful description of experimental results of baryon stopping, which is challenging to describe for other theoretical models, this supports the idea that our physical picture, where baryon stopping in heavy-ion collisions arises due to the stopping of valence quarks by a saturated target, is actually appropriate to describe the process close to midrapidity at RHIC and LHC energies. Within this picture, the saturated target provides an effective scale, namely the saturation scale Q_B , which exhibits a characteristic center-of-mass energy and nuclear density dependence, that appears to be consistent with observations from nature.

Based on the apparent success of this model it would be interesting to further extend the framework to include additional fluctuations of the charge deposition that arise from event-by-event realizations of the quark content of the colliding hadrons. It would also be interesting, if challenging, to make use of more recent developments in the CGC EFT [39, 53] and extend the present theoretical calculations beyond leading order accuracy.



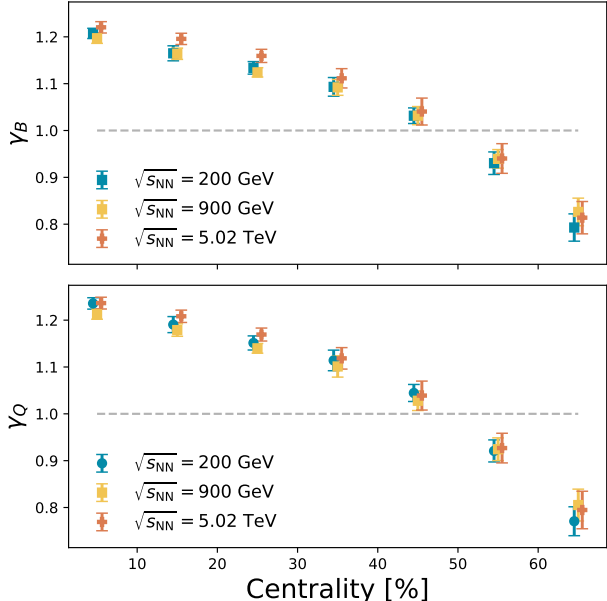


Figure 5: (top) Midrapidity baryon charge deposition as a function of nuclear mass number, A. The deposited charge follows a power law A^{γ_i} with i = [B, Q]. (Below) The baryon deposition parameter γ_i , found fitted from the McDipper. The parameter γ_i is independent of energy, but sensitive to centrality.

ACKNOWLEDGEMENTS

OGM would like to thank Nicole Lewis, Farid Salazar, David Frenklah and Travis Dore for productive discussions. This work is supported by the Deutsche Forschungsgemeinschaft (DFG, German Research Foundation) through the CRC-TR 211 'Strong-interaction matter under extreme conditions' — project number

315477589 — TRR 211. OGM and SS acknowledge also support by the German Bundesministerium für Bildung und Forschung (BMBF) through Grant No. 05P21PBCAA.

Appendix A: Beam-energy dependence of baryon stopping in collinear factorization

Below we use a dimensional analysis to obtain the center-of-mass energy (\sqrt{s}_{NN}) dependence of the netcharge deposition in collinearly factorized pQCD calculations at high energies. We first note that at leading order, quark charges are deposited via single scattering of collinear partons, and we consider a generic $h_1h_2 \to q_f X$ process, for which the cross-section is given by a convolution of the relevant PDFs $f_{i/h_j}(x,\mu)$ and the cross-section for the partonic sub-process as

$$\frac{\mathrm{d}\sigma^{h_1h_2 \to q_f X}}{\mathrm{d}^2 p_T \mathrm{d}y_q} = \sum_{ij} \int \mathrm{d}x_1 \, \mathrm{d}x_2 \, f_{i/h_1}(x_1, \mu) \, f_{j/h_2}(x_2, \mu)
\times \frac{\mathrm{d}\sigma^{ij \to q_f X}}{\mathrm{d}x_1 \mathrm{d}x_2 \mathrm{d}^2 p_T \mathrm{d}y_q}$$
(A1)

where p_T^q and y^q denote the transverse momentum and rapidity of the outgoing quark. Based on the cross-section for this process, we can then extract the net-quark yield by normalizing with the total inelastic cross section,

$$\frac{\mathrm{d}N^{h_1h_2\to q_fX}}{\mathrm{d}y_q} = \frac{1}{\sigma_{\mathrm{inel}}(s_{\mathrm{NN}})} \int \mathrm{d}^2p_T \frac{\mathrm{d}\sigma^{h_1h_2\to q_fg}}{\mathrm{d}^2p_T^q \mathrm{d}y_q} \quad (A2)$$

By kinematics the momentum fractions x_1 and x_2 determine the ratio of the hadronic center of mass energy $\sqrt{s_{NN}}$ to the center of mass energy of the partonic subprocess \sqrt{s} as

$$s = x_1 x_2 s_{\text{NN}} \tag{A3}$$

Now the differential cross-section for the partonic subprocess $\frac{\mathrm{d}\sigma^{ij\to q_f X}}{\mathrm{d}x_1\mathrm{d}x_2\mathrm{d}^2p_T^q\mathrm{d}y_q}$, is determined by the dimensionless variables x_1,x_2,y_q and the energy scales \sqrt{s} and p_T^q . In the limit where both of these scales $p_T^q,\sqrt{s}\gg\Lambda_{\rm QCD}$, dimensional analysis suggests that, up to an overall prefactor $1/s^2$ the cross-section can be expressed as in terms of a dimensionless function $\frac{\mathrm{d}\tilde{\sigma}^{ij\to q_f X}}{\mathrm{d}x_1\mathrm{d}x_2\mathrm{d}^2p_T\mathrm{d}y_q}\left(\frac{p_T^q}{\sqrt{s}}\right)$ of the ratio of these two scales, i.e.

$$\frac{\mathrm{d}\sigma^{ij\to q_fX}}{\mathrm{d}x_1\mathrm{d}x_2\mathrm{d}^2p_T^q\mathrm{d}y_q} = \frac{1}{s^2}\frac{\mathrm{d}\tilde{\sigma}^{ij\to q_fX}}{\mathrm{d}x_1\mathrm{d}x_2\mathrm{d}^2p_T\mathrm{d}y_q}\left(\frac{p_T^q}{\sqrt{s}}\right) \tag{A4}$$

By inserting this expression into Eq. (A1), we can absorb one power of 1/s to change the transverse momentum p_T^q integration, to an integration over the dimensionless variable $\frac{p_T^q}{\sqrt{s}}$, and use Eq. (A3) to express

$$\frac{\mathrm{d}N^{h_1h_2\to q_fX}}{\mathrm{d}y_q} = \frac{1}{\sigma_{\mathrm{inel}}(s_{\mathrm{NN}})s_{\mathrm{NN}}} \int \frac{\mathrm{d}x_1}{x_1} f_{i/h_1}(x_1,\mu) \int \frac{\mathrm{d}x_2}{x_2} f_{j/h_2}(x_2,\mu) \int \mathrm{d}^2\left(\frac{p_T^q}{\sqrt{s}}\right) \frac{\mathrm{d}\tilde{\sigma}^{ij\to q_fX}}{\mathrm{d}x_1\mathrm{d}x_2\mathrm{d}^2p_T\mathrm{d}y_q} \left(\frac{p_T^q}{\sqrt{s}}\right) \tag{A5}$$

In the high energy limit, $s_{\rm NN} \approx m_N \exp[y_{\rm beam}]$. Additionally, it is parametrically known that $\sigma_{\rm inel}(s_{\rm NN}) \approx \log^2(s_{\rm NN}) \sim y_{\rm beam}^2$. Baryon and electric charge can be then obtained by computing the some process for the antiquark and take the appropriate linear combination. The resulting exponent is then

$$\alpha_B \sim 2$$
 (A6)

which is qualitatively compatible to the event generator results discussed in Ref. [30].

A small caveat is in order: this result is valid as a very coarse approximation, but corrections will not change the qualitative behaviour $\alpha_B > 1$. The difference from this result to the once presented in the main text rest on the difference of kinematics. While here the scaling is solely driven by the momentum conservation of one scattering, the saturation results are prompted by the total momentum broadening of a charge through a medium which is described by a distribution with characteristic scale Q_S . Therefore, the so-called naive quark stopping comprises a very particular limit of the quark stopping picture.

- [1] M. Aaboud *et al.* (ATLAS), Measurement of longitudinal flow decorrelations in Pb+Pb collisions at $\sqrt{s_{\rm NN}} = 2.76$ and 5.02 TeV with the ATLAS detector, Eur. Phys. J. C 78, 142 (2018), arXiv:1709.02301 [nucl-ex].
- [2] P. Bozek and W. Broniowski, The torque effect and fluctuations of entropy deposition in rapidity in ultrarelativistic nuclear collisions, Phys. Lett. B **752**, 206 (2016), arXiv:1506.02817 [nucl-th].
- [3] H. Petersen, V. Bhattacharya, S. A. Bass, and C. Greiner, Longitudinal correlation of the triangular flow event plane in a hybrid approach with hadron and parton cascade initial conditions, Phys. Rev. C 84, 054908 (2011), arXiv:1105.0340 [nucl-th].
- [4] M. Nie (STAR), Measurement of longitudinal decorrelation of anisotropic flow V 2 and V 3 in 200 GeV Au+Au collisions at STAR, Nucl. Phys. A 982, 403 (2019).
- [5] V. Khachatryan et al. (CMS), Evidence for transverse momentum and pseudorapidity dependent event plane fluctuations in PbPb and pPb collisions, Phys. Rev. C 92, 034911 (2015), arXiv:1503.01692 [nucl-ex].
- [6] O. Savchuk and S. Pratt, Correlations of conserved quantities at finite baryon density, Phys. Rev. C 109, 024910 (2024), arXiv:2311.02046 [nucl-th].
- [7] J. A. Fotakis, M. Greif, C. Greiner, G. S. Denicol, and H. Niemi, Diffusion processes involving multiple conserved charges: A study from kinetic theory and implications to the fluid-dynamical modeling of heavy ion collisions, Phys. Rev. D 101, 076007 (2020), arXiv:1912.09103 [hep-ph].
- [8] D. Tlusty, The RHIC Beam Energy Scan Phase II: Physics and Upgrades, in 13th Conference on the Intersections of Particle and Nuclear Physics (2018) arXiv:1810.04767 [nucl-ex].
- [9] J. Brewer, S. Mukherjee, K. Rajagopal, and Y. Yin, Searching for the QCD critical point via the rapidity dependence of cumulants, Phys. Rev. C 98, 061901 (2018), arXiv:1804.10215 [hep-ph].
- [10] M. Li and J. I. Kapusta, Large Baryon Densities Achievable in High Energy Heavy Ion Collisions Outside the Central Rapidity Region, Phys. Rev. C 99, 014906 (2019), arXiv:1808.05751 [nucl-th].
- [11] L. Du, H. Gao, S. Jeon, and C. Gale, Rapidity scan with

- multistage hydrodynamic and statistical thermal models, Phys. Rev. C 109, 014907 (2024), arXiv:2302.13852 [nucl-th].
- [12] J. Li, L. Du, and S. Shi, Rapidity scan approach for net-baryon cumulants with a statistical thermal model, Phys. Rev. C 109, 034906 (2024), arXiv:2311.11374 [nucl-th].
- [13] M. Arslandok, S. A. Bass, A. A. Baty, I. Bautista, C. Beattie, F. Becattini, R. Bellwied, Y. Berdnikov, A. Berdnikov, J. Bielcik, J. T. Blair, et al., Hot QCD White Paper, (2023), arXiv:2303.17254 [nucl-ex].
- [14] Letter of Intent: A Forward Calorimeter (FoCal) in the ALICE experiment, (2020).
- [15] Letter of intent for ALICE 3: A next-generation heavyion experiment at the LHC, (2022), arXiv:2211.02491 [physics.ins-det].
- [16] H. Appelshauser et al. (NA49), Baryon stopping and charged particle distributions in central Pb + Pb collisions at 158-GeV per nucleon, Phys. Rev. Lett. 82, 2471 (1999), arXiv:nucl-ex/9810014.
- [17] I. G. Bearden et al. (BRAHMS), Nuclear stopping in Au + Au collisions at s(NN)**(1/2) = 200-GeV, Phys. Rev. Lett. 93, 102301 (2004), arXiv:nucl-ex/0312023.
- [18] J. Mohs, S. Ryu, and H. Elfner (SMASH), Particle Production via Strings and Baryon Stopping within a Hadronic Transport Approach, J. Phys. G 47, 065101 (2020), arXiv:1909.05586 [nucl-th].
- [19] A. Schäfer, I. Karpenko, X.-Y. Wu, J. Hammelmann, and H. Elfner (SMASH), Particle production in a hybrid approach for a beam energy scan of Au+Au/Pb+Pb collisions between $\sqrt{s_{NN}}=4.3$ GeV and $\sqrt{s_{NN}}=200.0$ GeV, Eur. Phys. J. A **58**, 230 (2022), arXiv:2112.08724 [hep-ph].
- [20] H. Weber, E. L. Bratkovskaya, and H. Stoecker, Baryon stopping and strange baryon and anti-baryon production at ultrarelativistic energies, Phys. Rev. C 66, 054903 (2002).
- [21] J. Hoelck and G. Wolschin, Baryon stopping as a relativistic Markov process in phase space, Phys. Rev. Res. 2, 033409 (2020), arXiv:2009.08913 [nucl-th].
- [22] C. Shen and B. Schenke, Dynamical initial state model for relativistic heavy-ion collisions, Phys. Rev. C 97, 024907 (2018), arXiv:1710.00881 [nucl-th].

- [23] D. Kharzeev, Can gluons trace baryon number?, Phys. Lett. B 378, 238 (1996), arXiv:nucl-th/9602027.
- [24] C. Shen and B. Schenke, Longitudinal dynamics and particle production in relativistic nuclear collisions, Phys. Rev. C 105, 064905 (2022), arXiv:2203.04685 [nucl-th].
- [25] D. Frenklakh, D. Kharzeev, G. Rossi, and G. Veneziano, Baryon-number — flavor separation in the topological expansion of QCD, JHEP 07, 262, arXiv:2405.04569 [hepph].
- [26] B. Andersson, G. Gustafson, G. Ingelman, and T. Sjostrand, Parton Fragmentation and String Dynamics, Phys. Rept. 97, 31 (1983).
- [27] T. Sjostrand, S. Mrenna, and P. Z. Skands, PYTHIA 6.4 Physics and Manual, JHEP 05, 026, arXiv:hepph/0603175.
- [28] S. Frixione, P. Nason, and G. Ridolfi, A Positive-weight next-to-leading-order Monte Carlo for heavy flavour hadroproduction, JHEP 09, 126, arXiv:0707.3088 [hep-ph].
- [29] G. Corcella, I. G. Knowles, G. Marchesini, S. Moretti, K. Odagiri, P. Richardson, M. H. Seymour, and B. R. Webber, HERWIG 6: An Event generator for hadron emission reactions with interfering gluons (including supersymmetric processes), JHEP 01, 010, arXiv:hepph/0011363.
- [30] N. Lewis, W. Lv, M. A. Ross, C. Y. Tsang, J. D. Brandenburg, Z.-W. Lin, R. Ma, Z. Tang, P. Tribedy, and Z. Xu, Search for baryon junctions in photonuclear processes and isobar collisions at RHIC, Eur. Phys. J. C 84, 590 (2024), arXiv:2205.05685 [hep-ph].
- [31] A. Dumitru and J. Jalilian-Marian, Forward quark jets from protons shattering the colored glass, Phys. Rev. Lett. 89, 022301 (2002), arXiv:hep-ph/0204028.
- [32] W. Ke, J. S. Moreland, J. E. Bernhard, and S. A. Bass, Constraints on rapidity-dependent initial conditions from charged particle pseudorapidity densities and two-particle correlations, Phys. Rev. C 96, 044912 (2017), arXiv:1610.08490 [nucl-th].
- [33] W. Zhao, S. Ryu, C. Shen, and B. Schenke, 3D structure of anisotropic flow in small collision systems at energies available at the BNL Relativistic Heavy Ion Collider, Phys. Rev. C 107, 014904 (2023), arXiv:2211.16376 [nucl-th].
- [34] O. Garcia-Montero, H. Elfner, and S. Schlichting, McDIPPER: A novel saturation-based 3+1D initial-state model for heavy ion collisions, Phys. Rev. C 109, 044916 (2024), arXiv:2308.11713 [hep-ph].
- [35] O. Garcia-Montero, H. Elfner, and S. Schlichting, Charge and energy deposition in the McDIPPER framework, PoS HardProbes2023, 054 (2024), arXiv:2311.03125 [hepph].
- [36] L. D. McLerran and R. Venugopalan, Computing quark and gluon distribution functions for very large nuclei, Phys. Rev. D 49, 2233 (1994), arXiv:hep-ph/9309289.
- [37] L. D. McLerran and R. Venugopalan, Gluon distribution functions for very large nuclei at small transverse momentum, Phys. Rev. D 49, 3352 (1994), arXiv:hep-

- ph/9311205.
- [38] L. D. McLerran and R. Venugopalan, Green's functions in the color field of a large nucleus, Phys. Rev. D 50, 2225 (1994), arXiv:hep-ph/9402335.
- [39] A. Dumitru, A. Hayashigaki, and J. Jalilian-Marian, The Color glass condensate and hadron production in the forward region, Nucl. Phys. A 765, 464 (2006), arXiv:hepph/0506308.
- [40] H. Mäntysaari, Scattering off the Color Glass Condensate, Ph.D. thesis, Jyvaskyla U. (2015), arXiv:1506.07313 [hep-ph].
- [41] T. Lappi and H. Mantysaari, Forward dihadron correlations in deuteron-gold collisions with the Gaussian approximation of JIMWLK, Nucl. Phys. A 908, 51 (2013), arXiv:1209.2853 [hep-ph].
- [42] K. J. Golec-Biernat and M. Wusthoff, Saturation in diffractive deep inelastic scattering, Phys. Rev. D 60, 114023 (1999), arXiv:hep-ph/9903358.
- [43] H. Kowalski and D. Teaney, An Impact parameter dipole saturation model, Phys. Rev. D 68, 114005 (2003), arXiv:hep-ph/0304189.
- [44] H. Kowalski, L. Motyka, and G. Watt, Exclusive diffractive processes at HERA within the dipole picture, Phys. Rev. D 74, 074016 (2006), arXiv:hep-ph/0606272.
- [45] T.-J. Hou et al., New CTEQ global analysis of quantum chromodynamics with high-precision data from the LHC, Phys. Rev. D 103, 014013 (2021), arXiv:1912.10053 [hepph].
- [46] H. Mäntysaari and P. Zurita, In depth analysis of the combined HERA data in the dipole models with and without saturation, Phys. Rev. D 98, 036002 (2018), arXiv:1804.05311 [hep-ph].
- [47] B. I. Abelev et al. (STAR), Systematic Measurements of Identified Particle Spectra in pp, d⁺ Au and Au+Au Collisions from STAR, Phys. Rev. C 79, 034909 (2009), arXiv:0808.2041 [nucl-ex].
- [48] L. Adamczyk et al. (STAR), Bulk Properties of the Medium Produced in Relativistic Heavy-Ion Collisions from the Beam Energy Scan Program, Phys. Rev. C 96, 044904 (2017), arXiv:1701.07065 [nucl-ex].
- [49] B. Abelev *et al.* (ALICE), Centrality determination of Pb-Pb collisions at $\sqrt{s_{NN}} = 2.76$ TeV with ALICE, Phys. Rev. C **88**, 044909 (2013), arXiv:1301.4361 [nucl-ex].
- [50] B. Abelev *et al.* (ALICE), Centrality dependence of π , K, p production in Pb-Pb collisions at $\sqrt{s_{NN}}=2.76$ TeV, Phys. Rev. C **88**, 044910 (2013), arXiv:1303.0737 [hep-ex]
- [51] Y. Mehtar-Tani and G. Wolschin, Stopping in central Pb + Pb collisions at SPS energies and beyond, EPL 94, 62003 (2011), arXiv:1102.3134 [hep-ph].
- [52] Tracking the baryon number with nuclear collisions, (2024), arXiv:2408.15441 [nucl-ex].
- [53] J. P. Blaizot, F. Gelis, and R. Venugopalan, High-energy pA collisions in the color glass condensate approach.
 2. Quark production, Nucl. Phys. A 743, 57 (2004), arXiv:hep-ph/0402257.